

See discussions, stats, and author profiles for this publication at: <https://www.researchgate.net/publication/264127473>

Toward Plasmonics with Nanometer Precision: Nonlinear Optics of Helium-Ion Milled Gold Nanoantennas

ARTICLE in NANO LETTERS · JULY 2014

Impact Factor: 13.59 · DOI: 10.1021/nl5019589 · Source: PubMed

CITATIONS

25

READS

123

15 AUTHORS, INCLUDING:



[Heiko Kollmann](#)

Carl von Ossietzky Universität Oldenburg

7 PUBLICATIONS 66 CITATIONS

[SEE PROFILE](#)



[Ralf Vogelgesang](#)

Carl von Ossietzky Universität Oldenburg

95 PUBLICATIONS 2,049 CITATIONS

[SEE PROFILE](#)



[Christoph Lienau](#)

Carl von Ossietzky Universität Oldenburg

262 PUBLICATIONS 4,259 CITATIONS

[SEE PROFILE](#)

Toward Plasmonics with Nanometer Precision: Nonlinear Optics of Helium-Ion Milled Gold Nanoantennas

Heiko Kollmann,[†] Xianji Piao,[‡] Martin Esmann,[†] Simon F. Becker,[†] Dongchao Hou,[†] Chuong Huynh,[§] Lars-Oliver Kautschor,[§] Guido Böske,[§] Henning Vieker,^{||} André Beyer,^{||} Armin Gölzhäuser,^{||} Namkyoo Park,[‡] Ralf Vogelgesang,[†] Martin Silies,^{*,†} and Christoph Lienau[†]

[†]Institute of Physics and Center of Interface Science, Carl von Ossietzky Universität Oldenburg, D-26129 Oldenburg, Germany

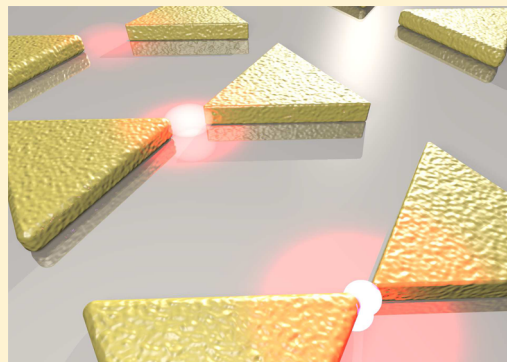
[‡]Photonic Systems Laboratory, School of Electrical Engineering, Seoul National University, 151-742 Seoul, Korea

[§]Carl Zeiss Microscopy GmbH, D-73447 Oberkochen, Germany

^{||}Faculty of Physics, Universität Bielefeld, D-33615 Bielefeld, Germany

Supporting Information

ABSTRACT: Plasmonic nanoantennas are versatile tools for coherently controlling and directing light on the nanoscale. For these antennas, current fabrication techniques such as electron beam lithography (EBL) or focused ion beam (FIB) milling with Ga⁺-ions routinely achieve feature sizes in the 10 nm range. However, they suffer increasingly from inherent limitations when a precision of single nanometers down to atomic length scales is required, where exciting quantum mechanical effects are expected to affect the nanoantenna optics. Here, we demonstrate that a combined approach of Ga⁺-FIB and milling-based He⁺-ion lithography (HIL) for the fabrication of nanoantennas offers to readily overcome some of these limitations. Gold bowtie antennas with 6 nm gap size were fabricated with single-nanometer accuracy and high reproducibility. Using third harmonic (TH) spectroscopy, we find a substantial enhancement of the nonlinear emission intensity of single HIL-antennas compared to those produced by state-of-the-art gallium-based milling. Moreover, HIL-antennas show a vastly improved polarization contrast. This superior nonlinear performance of HIL-derived plasmonic structures is an excellent testimonial to the application of He⁺-ion beam milling for ultrahigh precision nanofabrication, which in turn can be viewed as a stepping stone to mastering quantum optical investigations in the near-field.



KEYWORDS: *Nano-Optics, Helium-Ion Lithography, Plasmonics, Ultrafast Optics, Third Harmonic Spectroscopy*

Plasmonic nanostructures like metallic nanoantennas have been widely recognized as functional elements in a wide range of applications. Their intense evanescent fields are employed in the generation of femtosecond electron^{1,2} or extreme UV atomic line emission.³ The accompanying tight spatial localization of the near-field is routinely used in single-molecule spectroscopy,^{4–7} near-field or nanoscale imaging,^{6,8,9} and photovoltaic applications.^{10,11} Increasingly, plasmonic nanoantennas also attract attention in the context of quantum mechanical phenomena, however, which require delicate spatial alignment of field or material structures.¹² Consequently, the dependencies of linear and nonlinear optical properties of metallic nanoantennas on size and shape have been investigated extensively in the recent years.^{13–16}

A particular focus has been on so-called gap plasmons, which appear in the nanometer-sized void between two plasmonic antennas.^{5,17} These have been demonstrated to provide tremendous enhancement of the local electric field in the gap, thanks to the growth of near-field-mediated optical interactions.^{18–20} Aiming for such enhanced optical near fields

in nanoantenna structures, reproducible and precise fabrication techniques are indispensable.

Standard fabrication processes like focused ion beam (FIB) milling^{8,21–23} or photo resist-based electron beam lithography (EBL)^{13,14,24,25} have made great progress toward this goal, easily achieving lateral feature sizes between 10 and 20 nm. On one hand, Ga⁺ milling is limited in resolution to typically more than 10 nm and results in undesired Ga⁺-ion implantation at the interface.^{3,19,21,26} This affects both the structural quality at the milling interface, that is, the surface roughness, and the dielectric function of the plasmonic structures.²⁷

Photo-resist-based EBL, on the other hand, can in principle, also be used to fabricate single antennas or antenna arrays with sizes of well below 10 nm,^{28,29} in particular when using electron beams with kinetic energies well above 100 keV^{29,30} and special types of substrates such as thin SiN membranes. So far, however, very few of those samples have been fabricated and

Received: May 26, 2014

Revised: July 21, 2014

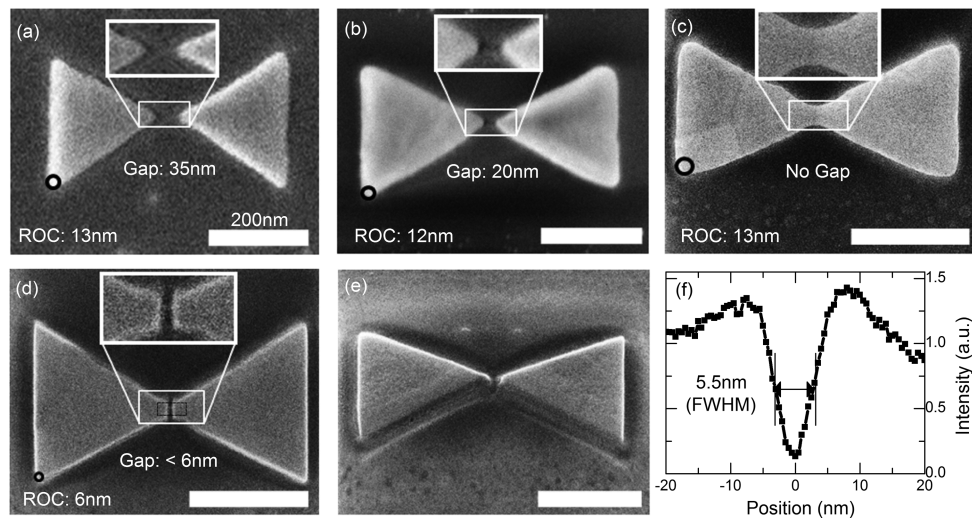


Figure 1. Scanning electron (a–c) and helium ion (d and e) microscopy images of bowtie nanoantennas fabricated by Ga^+ -ion (a–c) and He^+ -ion (d–f) beam milling. All antennas are milled into a 30 nm thick polycrystalline gold film evaporated onto a glass substrate. For Ga^+ milling, antenna gap sizes of some 35 nm are reached when directly using the Ga^+ image to optimize the beam focus. Smaller gap sizes of down to 20 nm are obtained in a sequential writing mode (b), using a series of imaging and milling steps for focus optimization. (c) Antenna without gap fabricated in sequential Ga^+ mode. In all cases, we find rounded corners with a radius of curvature (ROC) of about 13 nm. (d) Bowtie antenna fabricated by He^+ milling. A considerably reduced gap size of less than 6 nm and much sharper corners ($\text{ROC} \leq 6 \text{ nm}$) are obtained. (e) Side view of the same antenna (tilt angle 35°), showing the excellent aspect ratio reached by He^+ milling. (f) Cross section through the gap region of the image in (d), indicating a gap width of 5.5 nm. All scale bars are 200 nm long.

their nonlinear optical properties have not yet been investigated.

In response to these problems, milling-based He^+ -ion lithography (HIL)³¹ has recently been introduced as a resist-free milling technique for the fabrication of pristine nanostructures, potentially even with nanometer precision and better.³² Thanks to the chemical propensity of the noble gas for diffusion even out of solid matter, HIL reduces permanent contamination caused by inadvertently implanted ions or adhesion layers. An obvious disadvantage of HIL is the reduced milling speed due to the lighter ions in comparison with Ga^+ -ion milling. In practice, a combination of a first, coarse writing step by EBL or Ga^+ -ion milling with a second, HIL-based fine milling step may largely overcome this limitation. In this way, HIL provides a significant advance in spatial resolution and lateral smoothness. HIL machines already achieved sub-10 nm feature sizes and produced plasmonic nanoantennas with gaps of just a few nanometers.^{33–35} So far, however, nonlinear optical properties of HIL-fabricated nanostructures have not yet been investigated, and direct optical studies of their crucial local field enhancement are still lacking.

In this Letter, we present first evidence for the superior nonlinear optical performance of plasmonic nanostructures fabricated by a combination of Ga^+ - and He^+ -ion milling. Specifically, we study bowtie antennas with sub-6 nm gap sizes of unprecedented aspect ratio. Polarization and spectrally resolved nonlinear optical microscopy studies clearly demonstrate that the nonlinear emission—a highly sensitive indicator of local variations in electric field strength—is largely enhanced by field localization within the few-nanometer-sized antenna gap. Finite element method (FEM) simulations of the interaction of light with the bowtie structures strongly support this conclusion. HIL-antennas are found to emit a substantially enhanced third harmonic intensity and show a considerably

improved polarization contrast when compared with structures produced by state-of-the-art Ga^+ -FIB.

In order to compare the milling fidelity and yield of the novel He^+ -ion beam lithography with standard techniques like Ga^+ -FIB, we fabricate arrays of equilateral bowtie antennas from a 30 nm thick gold film, evaporated on a glass substrate (see Supporting Information). Examples of four typical antenna geometries used in the present study are shown in Figure 1a–e. In a first fabrication approach, we used a direct writing mode with Ga^+ -ions in an FEI Helios Nanolab 600i Dual Beam Microscope. Here, the ions were used for imaging of the sample surface, that is, small particles on the surface, to find the best focal parameters for the ion beam. This results in antennas with gap sizes down to 35 nm as can be seen in Figure 1a. In a second, sequential mode, we first optimize the focal parameters by direct imaging, then write a test structure, which then is imaged using SEM. We iteratively improve the focusing until we achieve optimum resolution of the test structure. This leads to a clear reduction of the achievable feature size and in particular to gap sizes of about 20 nm (Figure 1b). For studying the field localization within the gap region in detail and to facilitate a broader comparison, we thirdly fabricated fused antennas without a gap (Figure 1c). For all three milling protocols, the fabricated antenna structures show rounded corners, well characterized by a radius of curvature (ROC) of about 13 nm, only marginally smaller than reported for standard Ga^+ -FIB.³ The radii are however inherently limited by the beam size as well as the wide damage cascade in the surface-near volume.^{36,37} The problem can be addressed by using light ions like helium, with an atomic mass more than 1 order of magnitude smaller compared to Ga^+ . Apart from the smaller possible beam size, this leads to a substantially narrower damage cascade in the surface-near volume due to a smaller scattering rate and an increased penetration depth of several hundreds of nanometers. As a consequence, the removal rate of gold atoms from the surface is reduced, leading to a drastic

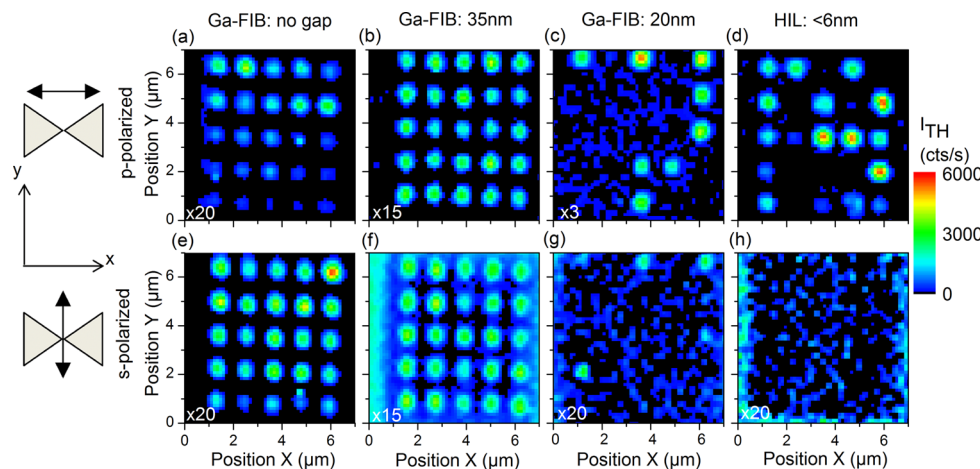


Figure 2. Spatially resolved maps of the third harmonic emission (TH) intensity of arrays of bowtie antennas after excitation with ultrabroadband *p*-polarized (a–d) and *s*-polarized (e–h) laser pulses centered around 920 nm and with an average power of 110 μW . The images represent results obtained for Ga⁺-FIB bowties without gap (a and e), with 35 nm gaps (b and f) and with 20 nm gaps (c and g). In (d) and (h), corresponding results for bowties fabricated by He⁺ milling and with gap distances of about 6 nm are shown. For the HIL antennas, a markedly enhanced polarization contrast is observed. The TH intensities in all images are normalized to a maximum intensity of 6000 cts/s. The corresponding normalization factors are given.

increase in milling time, accompanied by deposition of helium ions in the substrate.

In view of these considerations, we introduce a new, combined approach of first Ga⁺-ion beam milling of a fused antenna as shown in Figure 1c. In the second step, the gap is cut and its edges are sharpened using the He⁺-ion beam in a Carl Zeiss Orion Plus Microscope. This new nanofabrication and imaging tool is used for both imaging and structuring of the plasmonic antennas. With this new, two-stage milling protocol, the high production speed of the Ga⁺-FIB can be adopted and the implantation of Ga⁺-ions in the nanostructure is avoided. The exceptional quality of the He⁺ milled structures is evident from the helium ion microscopy (HIM) images presented in Figure 1d and e, which show a gap size of less than 6 nm, remarkably reduced compared to the other two Ga⁺ milled (Figure 1a,b) antenna structures. The excellent height-to-width aspect ratio of about 3.6 achievable by helium milling is illustrated in Figure 1e, where the tilted side view demonstrates that the He⁺ milling step reaches all the way down to the substrate surface. The outstandingly small gap and the small ROC of the fabricated antennas in comparison to the best Ga⁺-FIB antennas can be seen in the HIM cross section taken along the gap region indicated by the dashed boxes (Figure 1f). Clearly, the nanometer milling accuracy of HIL results in a substantial sharpening of the edges, steeper walls, and corners with a radius of curvature of only about 6 nm.

To directly determine the optical field enhancements in bowtie antennas, linear^{38,39} as well as nonlinear^{14,40,41} optical spectroscopy may be used. However, the observation of small variations in the local field enhancement of single antennas is fairly challenging in linear measurements due to a small contribution to the overall antenna emission. In contrast, nonlinear optical phenomena offer much higher sensitivity and contrast in detecting small variations in local field enhancement. When recording, for example, the third harmonic (TH) of the incident light, the TH intensity is proportional to the sixth power of the local electric field and $I_{\text{TH,loc}}(3\omega, \vec{r}) \propto |E_{\text{loc}}(\omega, \vec{r})|^6$ represents an exquisite measure of the local field concentration at position \vec{r} within the nanoantennas. For the purpose of this Letter, we define the local field enhancement

factor $L_{\text{loc}}(\omega, \vec{r})$ as the ratio of the local electric field $\vec{E}_{\text{local}}(\omega, \vec{r})$ and the spatially homogeneous incident electric field $\vec{E}_0(\omega)$, that is, $L_{\text{loc}}(\omega, \vec{r}) = |\vec{E}_{\text{loc}}(\omega, \vec{r})|/|\vec{E}_0(\omega)|$. This local field enhancement depends on the overall plasmonic resonance given by the material composition and geometric parameters of the antenna. However, it can be further increased at surface areas of large local curvature. This so-called lightning rod effect compresses the electric field at edges and corners into small, nanometer-sized volumes inside and near the surface of the plasmonic structure, leading to intense signals at the third harmonic frequency.

In our optical experiment, we measure the field localization using a home-built, ultrabroadband TH microscope. A Ti:sapphire laser system (Venteon: Pulse: ONE) delivers ultrashort laser pulses in the visible to near-infrared spectral range (650–1200 nm), centered around 920 nm with a pulse duration of about 8 fs at a repetition rate of 80 MHz. The laser pulses are dispersion-compensated and focused onto the sample surface to a diameter of about 1 μm (see Supporting Information). The time structure of the 8 fs focused pulses is preserved by using all reflective optics.^{42,43} Third harmonic emission is collected in back-reflection geometry, spectrally dispersed in a 50 cm monochromator (Acton SpectraPro-2500i), and detected with a liquid nitrogen cooled charge coupled device camera (Princeton Instruments Spec-10).

In Figure 2, spectrally integrated TH maps, that is, $I_{\text{TH}}(x, y)$, recorded from arrays of the four antenna geometries milled by He⁺- and Ga⁺-ion beam lithography are shown. All measurements are performed at an average excitation power of 110 μW . The top row displays maps recorded with *p*-polarized (\vec{E}_0 parallel to the bowtie axis; Figure 2a) and the bottom row with *s*-polarized excitation (\vec{E}_0 perpendicular to the bowtie axis; Figure 2e). The same color scale is applied to all panels with corresponding normalization factors given in the maps.

Evidently, differently fabricated antennas respond with drastically different TH emission to the change of the excitation polarization resulting in a drastic variation of the polarization contrast $I_{\text{TH,p-pol}}/I_{\text{TH,s-pol}}$. For the antennas with no gap (Figure 2a and e) and a gap of 35 nm (Figure 2b and f) the overall TH emission is rather low and the polarization contrast ratio is

close to 1, indicating that the structures are nearly insensitive to changes of the excitation polarization. Reducing the gap size to 20 nm using the sequential writing mode leads both to an overall increase of I_{TH} by a factor of 5 for *p*-polarized light (Figure 2c) and a modest decrease for *s*-polarized excitation (Figure 2g), resulting in an improved polarization contrast of 13:1. The TH intensity emitted by the He⁺ milled structures further increases for *p*-polarized excitation (Figure 2d) and decreases for *s*-polarized light (Figure 2h). The superb contrast ratio of more than 100:1 is limited here by detector noise. This enhancement in TH emission and the concomitant near-perfect polarization contrast are significant indicators for the enhanced near-field coupling between both triangles induced exclusively by the reduced gap size of the HIL antenna.¹³ Evidently, some of the antennas in Figure 2 are showing a much reduced THG signal. There are different possible reasons for this strong quenching of the THG signal, including an incomplete removal of gold from the gap region, possible effects of grain boundaries in the gap region on the gap geometry and laser-induced thermal damage.⁴⁴ Extinction spectra of single nanostructures indeed show that an incomplete removal of gold from the gap region strongly blue-shifts the resonance and suppresses THG in several of the investigated antennas.

We now investigate the optical response to *p*-polarized excitation of *single*, Ga⁺- or He⁺-ion produced antennas with gap sizes of 35, 20, and less than 6 nm. First, we detect the spectrally integrated TH for emission wavelengths between 270 and 330 nm while varying the average laser power on the sample between 33 and 300 μW . Because the excitation spot of $1 \mu\text{m}^2$ is larger than the footprint of a single bowtie antenna, we are sensitive only to the spatially integrated bowtie emission, that is, $I_{\text{TH}} \propto \int_{\omega} \int_{\text{bowtie volume}} E_{\text{TH, loc}}(\vec{r}, \omega) d^3 r d\omega$. In Figure 3a, the measured power dependence of I_{TH} from single bowties with gap sizes of about 35 nm (red triangles), 20 nm (black squares), and less than 6 nm for the HIL process (blue circles) are illustrated on a double-logarithmic scale. The emission dependencies for low-power measurements can be described by a cubic function, indicating a three-photon process as expected for TH generation. The bowtie fabricated by the direct writing mode shows only weak TH emission of a few 100 cts/s at laser powers below 100 μW . However, the bowties from the sequential Ga⁺-FIB writing mode with a gap size of 20 nm generate a five times higher TH signal. Here, excitation powers of more than 140 μW already induce an irreversible change in the optical response, likely due to melting or ablation processes that affect the vicinity of the gap.^{3,18,45} The highest TH emission, however, is measured from the HIL antenna, which is another factor of 3 larger than the signals from the best Ga⁺-FIB bowties. Here, permanent damage sets in at an excitation power of 100 μW . Again, this is in good agreement with the TH emission enhancement measured from antenna arrays shown in Figure 2. From this result, we can therefore estimate a spatially averaged relative field enhancement at the fundamental wavelength of $(I_{\text{TH,6nm}}/I_{\text{TH,20nm}})^{1/6} = 1.2$ when decreasing the gap from 20 to 6 nm. This rise of the spatially averaged field enhancement occurs even though the electric field for the He⁺-ion milled antenna is confined to a significantly smaller volume than for the Ga⁺-ion produced bowties.

To further confirm the finding that the field localization is taking place predominantly in the gap region of the bowtie antenna, we have performed detailed polarization-sensitive TH measurements of a single He⁺-ion produced antenna structure. In Figure 3b, the TH intensities recorded from one of the most

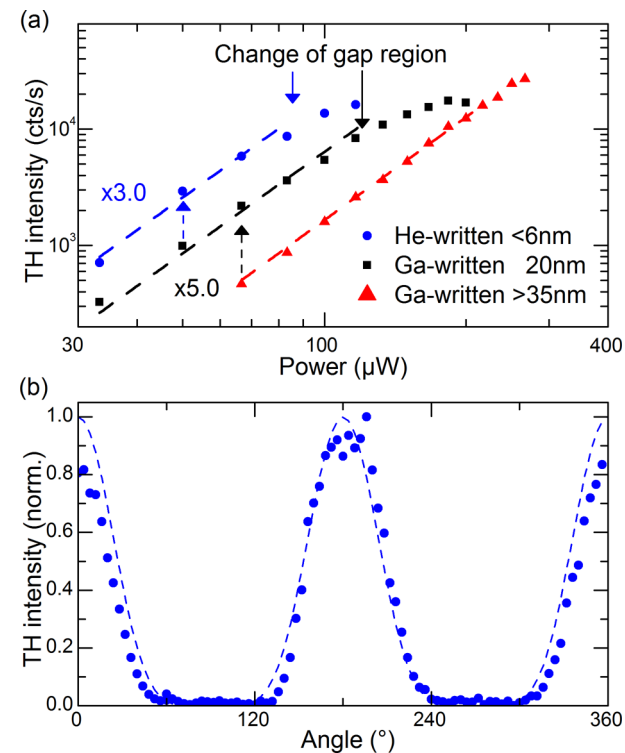


Figure 3. TH intensities as a function of excitation power recorded from individual bowtie antennas fabricated by direct Ga⁺ milling (gap distance >35 nm, red triangles), by sequential Ga⁺ milling (20 nm, black squares), and by He⁺ milling (6 nm, blue circles). All experiments were performed with 8 fs laser pulses, linearly polarized along the bowtie axis, from a Ti:sapphire oscillator centered at 920 nm. All curves show, for sufficiently low excitation intensities, a cubic power dependence of the TH intensity (dashed lines). The TH intensity of the bowties written by He⁺ milling is three times higher than that of the best antennas written by Ga⁺ milling, despite the smaller area of the gap region. (b) Dependence of the TH intensities on the polarization direction of the linearly polarized incident light for an antenna fabricated by He⁺-ion beam lithography. The data (blue circles) show a clean $\cos(\theta)^6$ dependence of the TH intensity on the polarization angle θ and a suppression of the TH intensity by more than a factor of 200 for an incident polarization perpendicular to the bowtie axis.

intense HIL-antennas at an excitation power of 100 μW are presented as a function of the excitation polarization angle θ (blue circles). The angle-dependent, spectrally integrated intensity is very closely proportional to $I_{\text{TH}}(\theta) \sim (\cos^2(\theta))^3 = \cos^6(\theta)$ indicated by the blue-dashed line. Evidently, pronounced dipolar resonances along the long horizontal and the short vertical axis of the antenna exist, which are spectrally clearly separated.^{13,46,47} The remarkable polarization contrast of more than 200:1, limited by background noise of the signal detection, indicates that the gap region responds exclusively to polarization along the bowtie axis and is hardly excited under perpendicular polarization.

Our experimental findings discussed above strongly suggest that the electric field localizes mainly in the gap region of the bowtie antenna. To lend further support to this conclusion, we perform detailed three-dimensional finite-element-method (FEM) simulations. In these, the refractive index of gold is taken from Palik⁴⁸ and the substrate is described by a constant refractive index of $n = 1.76$. We choose a spatially homogeneous, horizontally polarized incident electric field,

pointing along the x axis, and calculate the local near-field distribution $E_x(\lambda, x, y)$ at half height of the 30 nm thick gold structures for an incident wavelength λ at lateral position (x, y) . In Figure 4a, near-field intensity spectra $I(\lambda) = \int |E_x(\lambda, x, y, z)|^2 dx dy$

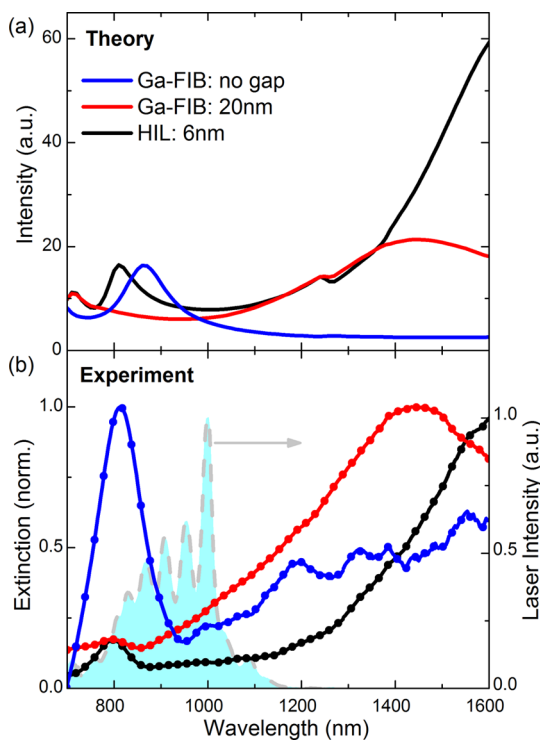


Figure 4. (a) Calculated near-field intensity spectra of gold bowtie nanoantennas on a glass substrate. The antenna geometries of the 6 nm gap He⁺-FIB antenna (black), the 20 nm gap Ga⁺-FIB antenna (red), and the no-gap Ga⁺-FIB antenna (blue) are taken from Figure 1. The near-field intensity spectra $I(\lambda) = \int |E_x(\lambda, x, y, z = 15 \text{ nm})|^2 dx dy$ are calculated at center height ($z = 15 \text{ nm}$) of the 30 nm thick antennas and for p polarization of the incident light. (b) Representative optical extinction spectra of a single 6 nm gap He⁺-FIB antenna (black circles), a single 20 nm gap Ga⁺-FIB antenna (red circles), and a single Ga⁺-FIB antenna without gap (blue circles). The spectra are recorded using a halogen lamp with p -polarized incident light. The maximum extinction in each spectrum is normalized to unity. Note the pronounced red shift of the He⁺-FIB antenna resonance. The spectrum of the 8 fs laser used in the nonlinear optical experiments is shown as a blue-shaded background. Its intensity is given on the right-hand axis of the panel, as indicated by the gray arrow.

$15 \text{ nm})^2 dx dy$ are displayed for three different antenna geometries, that is, without gap (blue line), and with a gap size of 20 nm (red line) and 6 nm (black line). These spectra are compared to representative optical extinction spectra of a single 6 nm gap He⁺-FIB antenna (black circles), a single 20 nm gap Ga⁺-FIB antenna (red circles), and a single Ga⁺-FIB antenna without gap (blue circles) in Figure 4b. The experimental excitation spectrum is shown as a blue-shaded background in (b). In general, the measured spectra are convincing agreement with the simulations. Both, the spectral positions of the different resonances and their optical line width match reasonably well. In particular, the pronounced red shift of the bright dipolar mode of the He⁺-FIB antenna by more than 200 nm compared to the Ga⁺-FIB antenna bowtie with a 20 nm gap is confirmed experimentally. Predominantly, this red-shift can be attributed to an increased near-field coupling of the two

triangles of the antenna when decreasing the gap size. As a consequence of the small gap, the coupled bowtie antennas form hybridized modes, that is, a blue-shifted dipolar dark or antibonding mode and a red-shifted dipolar bright or bonding mode. The very strong red shift of the bright dipolar mode of the He⁺-FIB that is seen in Figure 4b evidence the pronounced near-field coupling in this antenna and, hence, its excellent structural and optical properties.

As can be seen from these spectra, the fabricated antennas are off-resonantly excited in the nonlinear optical experiments reported in Figures 2 and 3. To account for this off-resonant laser excitation, panels a–c of Figure 5 now illustrate maps of the local electric field enhancement $L_{\text{nres}}(x, y) = \langle |E_x(x, y, z = 15 \text{ nm})| \rangle / \langle |E_0| \rangle$, averaged over the spectrum of the 8 fs laser pulses used in the experiment. The color scale of $L_{\text{nres}}(x, y)$ is kept constant between the main panels. The inset of each map shows a zoom into the gap region on a different, logarithmic color scale to display the full range of the local field enhancement. The calculations clearly show that the field enhancement around all antennas is localized mainly at their respective center. The maximum field enhancement varies strongly among the structures, with the strongest field enhancement (about 100 \times) being found for the 6 nm gap structure. Even though the excitation radiation is far off its main resonance, the field enhancement is about three times as strong as for the structure with a gap size of 20 nm and about five times stronger than for the gapless antenna. In general, the observed trend of increasing field enhancement for decreasing antenna gap sizes qualitatively reflects our experimental findings from Figure 3a, in which the TH emission was taken as a spatially averaged measure for the local field enhancement.

The simulations also suggest an option for increasing the field enhancement even further: In Figure 5d–f, the local near-field enhancement is shown when exciting the three bowtie antennas at their respective resonance, as depicted in Figure 4a. The bowtie structure without gap shown in Figure 5d exhibits a weak enhancement, spatially distributed over a broad range and with peak values well below 20. For the 20 nm gap Ga⁺-FIB structure shown in Figure 5e, the local field enhancement increases drastically to more than 80, sharply concentrated in the vicinity of the gap. However, the largest enhancement is again found for the 6 nm gap structure shown in Figure 5f. Here, the spatial field localization increases even more and reaches an electric field amplitude more than 300 times the incident field, more than a factor of 3 larger than for our experimental, off-resonant excitation. We point out that the electric field is furthermore exquisitely homogeneous within the 6 nm gap region, forming a capacitor-like field of exceptionally large amplitude. Given the excellent aspect ratio demonstrated in Figure 1f, the bowtie antenna essentially acts as a nanoscopic parallel plate capacitor with sidewall areas of approximately $30 \times 30 \text{ nm}^2$ and a separation of only 6 nm. This makes it a particularly attractive nanocavity for localizing electromagnetic fields with well-defined polarization properties to nanometric volumes and to explore their enhanced coupling to nan emitters.

Further evidence that the strong correlation of TH emission with bowtie gap size is more than an empirical connection is found in the consideration of the material origins of TH emission. We determine the spatially averaged field enhancement in the FEM calculations from the region, in which the field is the most dominant, that is, the area near the antenna edges. Because TH emission is expected only from the antenna

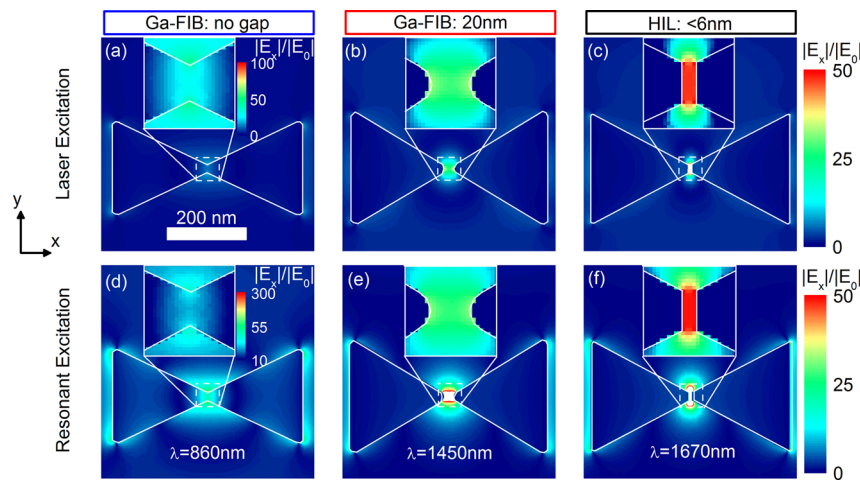


Figure 5. Calculated two-dimensional near-field distributions from gold bowtie nanoantennas on a glass substrate. These geometries are taken from the images in Figure 1. (a–c) Local near-field enhancement $L_{\text{res}}(x, y) = \langle |E_x(x, y, z = 15 \text{ nm})| \rangle / \langle |E_0| \rangle$ averaged over the spectrum of the incident 8 fs laser pulse. In the insets, $L_{\text{res}}(x, y)$ is plotted on a logarithmic scale. Note the pronounced and spatially homogeneous local field enhancement in the gap region of the He^+ antenna. (d–f) Resonant local near-field enhancement $L_{\text{res}}(x, y) = |E_x(\lambda_{\text{res}}, x, y, z = 15 \text{ nm})| / |E_0|$ calculated for monochromatic *p*-polarized incident light at the dominant resonance wavelength λ_{res} of the antenna structure (Figure 1). The corresponding resonance wavelength is indicated in each panel.

material, not the surrounding air, we limit our integration over the field enhancement to the metal area. We find a factor of 1.3 for the spatially averaged increase of the field enhancement, which is in good agreement with the experimentally determined value of 1.2.

In order to finally address the question whether the increase of TH emission for the HIL bowties is related to the increase of field enhancement or to the absence of Ga implantation by using the helium ion beam, we have performed additional FEM simulations in which the Ga⁺-FIB-written gold bowtie with a gap of 20 nm is adjusted by an additional 10 nm thick layer consisting of an alloy of 95% gold and 5% gallium. The comparison of the optical field enhancement of these bow-ties show, that the influence of the Ga contamination reduces the electric field enhancement by less than 10%, indicating that the increase of field enhancement for the HIL-fabricated bowties is mostly due to the reduced gap size.

In conclusion, the combination of Ga⁺- and He⁺-ion milling provides an unprecedented, few-nanometer milling precision for the fabrication of plasmonic nanostructures. By using nonlinear spectroscopy, we find markedly superior characteristics for plasmonic bowtie antennas fabricated by such a combined approach in contrast to conventional Ga⁺-FIB fabrication. He⁺-ion fabrication thus affords a considerable reduction of gap size, resulting in a significant increase of third harmonic emission and, importantly, outstanding polarization contrast. The finite element method calculations not only support these findings. Specifically, for the He⁺-ion produced bowtie antennas, they also indicate remarkably homogeneous electric field distributions within the few-nanometer gap volumes, reminiscent of nanocapacitors. The ability to control material structure features at the single-nanometer level makes He⁺-ion fabrication a prime candidate for the reliable fabrication of nanocavities. The profound electric field localization and the spatially highly homogeneous polarization properties of the localized fields suggest such bowtie nanostructures as prototypical structures for enhancing local vacuum field fluctuations and for probing the strong coupling between surface plasmon polariton fields and single quantum

emitters.⁴⁹ Experimental work in this direction is currently underway in our laboratory.

■ ASSOCIATED CONTENT

S Supporting Information

A more detailed description of (i) the sample preparation, (ii) nonlinear optical TH microscope setup, and (iii) the finite element modeling scheme. This material is available free of charge via the Internet at <http://pubs.acs.org>.

■ AUTHOR INFORMATION

Corresponding Author

*E-mail: martin.silics@uni-oldenburg.de.

Notes

The authors declare no competing financial interest.

■ ACKNOWLEDGMENTS

Financial support by the European Union project CRONOS (Grant number 280879-2), the Deutsche Forschungsgemeinschaft (SPP1391, DFGLiS80/8-1, INST184/107-1), and the Korea Foundation for International Cooperation of Science and Technology (Global Research Laboratory project, K20815000003) is gratefully acknowledged.

■ REFERENCES

- (1) Kubo, A.; Onda, K.; Petek, H.; Sun, Z.; Jung, Y. S.; Kim, H. K. *Nano Lett.* **2005**, 5 (6), 1123–1127.
- (2) Ropers, C.; Solli, D. R.; Schulz, C. P.; Lienau, C.; Elsaesser, T. *Phys. Rev. Lett.* **2007**, 98 (4), 043907.
- (3) Sivis, M.; Duwe, M.; Abel, B.; Ropers, C. *Nat. Phys.* **2013**, 9 (5), 304–309.
- (4) Punj, D.; Mivelle, M.; Moparthi, S. B.; van Zanten, T. S.; Rigneault, H.; van Hulst, N. F.; Garcia-Parajo, M. F.; Wenger, J. *Nat. Nano* **2013**, 8 (7), 512–516.
- (5) Schuller, J. A.; Barnard, E. S.; Cai, W.; Jun, Y. C.; White, J. S.; Brongersma, M. L. *Nat. Mater.* **2010**, 9 (3), 193–204.
- (6) Bharadwaj, P.; Deutsch, B.; Novotny, L. *Adv. Opt. Photon.* **2009**, 1 (3), 438–483.
- (7) Taminiua, T. H.; Moerland, R. J.; Segerink, F. B.; Kuipers, L.; van Hulst, N. F. *Nano Lett.* **2006**, 7 (1), 28–33.

- (8) Farahani, J. N.; Pohl, D. W.; Eisler, H. J.; Hecht, B. *Phys. Rev. Lett.* **2005**, *95* (1), 017402.
- (9) Farahani, J. N.; Eisler, H. J.; Pohl, D. W.; Pavius, M.; Flückinger, P.; Gasser, P.; Hecht, B. *Nanotechnology* **2007**, *18* (12), 125506.
- (10) Catchpole, K. R.; Polman, A. *Opt. Express* **2008**, *16* (26), 21793–21800.
- (11) Atwater, H. A.; Polman, A. *Nat. Mater.* **2010**, *9* (3), 205–213.
- (12) Savage, K. J.; Hawkeye, M. M.; Esteban, R.; Borisov, A. G.; Aizpurua, J.; Baumberg, J. J. *Nature* **2012**, *491* (7425), 574–577.
- (13) Hanke, T.; Cesar, J.; Knittel, V.; Trügler, A.; Hohenester, U.; Leitenstorfer, A.; Bratschitsch, R. *Nano Lett.* **2012**, *12* (2), 992–996.
- (14) Hanke, T.; Krauss, G.; Träutlein, D.; Wild, B.; Bratschitsch, R.; Leitenstorfer, A. *Phys. Rev. Lett.* **2009**, *103* (25), 257404.
- (15) Rechberger, W.; Hohenau, A.; Leitner, A.; Krenn, J. R.; Lamprecht, B.; Aussenegg, F. R. *Opt. Commun.* **2003**, *220* (1–3), 137–141.
- (16) Muskens, O. L.; Giannini, V.; Sánchez-Gil, J. A.; Gómez Rivas, J. *Opt. Express* **2007**, *15* (26), 17736–17746.
- (17) Siegfried, T.; Ekinci, Y.; Martin, O. J. F.; Sigg, H. *Nano Lett.* **2013**, *13* (11), 5449–5453.
- (18) Schuck, P. J.; Fromm, D. P.; Sundaramurthy, A.; Kino, G. S.; Moerner, W. E. *Phys. Rev. Lett.* **2005**, *94* (1), 017402.
- (19) Mühlischlegel, P.; Eisler, H. J.; Martin, O. J. F.; Hecht, B.; Pohl, D. W. *Science* **2005**, *308* (5728), 1607–1609.
- (20) Metzger, B.; Hentschel, M.; Schumacher, T.; Lippitz, M.; Ye, X.; Murray, C. B.; Knabe, B.; Buse, K.; Giessen, H. *Nano Lett.* **2014**.
- (21) Huang, J.-S.; Kern, J.; Geisler, P.; Weinmann, P.; Kamp, M.; Forchel, A.; Biagioni, P.; Hecht, B. *Nano Lett.* **2010**, *10* (6), 2105–2110.
- (22) Kim, S.; Jin, J.; Kim, Y.-J.; Park, I.-Y.; Kim, Y.; Kim, S.-W. *Nature* **2008**, *453* (7196), 757–760.
- (23) Sivis, M.; Duwe, M.; Abel, B.; Ropers, C. *Nature* **2012**, *485* (7397), E1–E3.
- (24) Muskens, O. L.; Giannini, V.; Sánchez-Gil, J. A.; Gómez Rivas, J. *Nano Lett.* **2007**, *7* (9), 2871–2875.
- (25) Koh, A. L.; Fernández-Domínguez, A. I.; McComb, D. W.; Maier, S. A.; Yang, J. K. W. *Nano Lett.* **2011**, *11* (3), 1323–1330.
- (26) Huang, J.-S.; Callegari, V.; Geisler, P.; Brüning, C.; Kern, J.; Prangsma, J. C.; Wu, X.; Feichtner, T.; Ziegler, J.; Weinmann, P.; Kamp, M.; Forchel, A.; Biagioni, P.; Sennhauser, U.; Hecht, B. *Nat. Commun.* **2010**, *1*, 150.
- (27) Ocelic, N.; Hillenbrand, R. *Nat. Mater.* **2004**, *3* (9), 606–609.
- (28) Duan, H.; Hu, H.; Kumar, K.; Shen, Z.; Yang, J. K. W. *ACS Nano* **2011**, *5* (9), 7593–7600.
- (29) Duan, H.; Fernández-Domínguez, A. I.; Bosman, M.; Maier, S. A.; Yang, J. K. W. *Nano Lett.* **2012**, *12* (3), 1683–1689.
- (30) Grigorescu, A. E.; Hagen, C. W. *Nanotechnology* **2009**, *20* (29), 292001.
- (31) Ward, B. W.; Notte, J. A.; Economou, N. P. *J. Vac. Sci. Technol., B: Microelectron. Nanometer Struct.–Process., Meas., Phenom.* **2006**, *24* (6), 2871–2874.
- (32) Bell, D. C.; Lemme, M. C.; Stern, L. A.; Williams, J. R.; Marcus, C. M. *Nanotechnology* **2009**, *20* (45), 455301.
- (33) Melli, M.; Polyakov, A.; Gargas, D.; Huynh, C.; Scipioni, L.; Bao, W.; Ogletree, D. F.; Schuck, P. J.; Cabrini, S.; Weber-Bargioni, A. *Nano Lett.* **2013**, *13* (6), 2687–2691.
- (34) Scholder, O.; Jefimovs, K.; Shorubalko, I.; Hafner, C.; Sennhauser, U.; Bona, G.-L. *Nanotechnology* **2013**, *24* (39), 395301.
- (35) Wang, Y.; Abb, M.; Boden, S. A.; Aizpurua, J.; de Groot, C. H.; Muskens, O. L. *Nano Lett.* **2013**, *13* (11), 5647–5653.
- (36) Notte, J. A. *Microscopy Today* **2012**, *20* (05), 16–22.
- (37) Hill, R.; Notte, J. A.; Scipioni, L. Scanning Helium Ion Microscopy. In *Advances in Imaging and Electron Physics*; Peter, W. H., Ed.; Elsevier: Amsterdam, 2012; Vol. 170, Ch. 2, pp 65–148.
- (38) Novotny, L.; van Hulst, N. *Nat. Photon* **2011**, *5* (2), 83–90.
- (39) Tang, L.; Kocabas, S. E.; Latif, S.; Okyay, A. K.; Ly-Gagnon, D.-S.; Saraswat, K. C.; Miller, D. A. B. *Nat. Photon* **2008**, *2* (4), 226–229.
- (40) Kauranen, M.; Zayats, A. V. *Nat. Photon* **2012**, *6* (11), 737–748.
- (41) Hentschel, M.; Utikal, T.; Giessen, H.; Lippitz, M. *Nano Lett.* **2012**, *12* (7), 3778–3782.
- (42) Piglosiewicz, B.; Sadiq, D.; Mascheck, M.; Schmidt, S.; Silies, M.; Vasa, P.; Lienau, C. *Opt. Express* **2011**, *19* (15), 14451–14463.
- (43) Mascheck, M.; Schmidt, S.; Silies, M.; Yatsui, T.; Kitamura, K.; Ohtsu, M.; Leipold, D.; Runge, E.; Lienau, C. *Nat. Photon* **2012**, *6* (5), 293–298.
- (44) Pfullmann, N.; Noack, M.; Cardoso de Andrade, J.; Rausch, S.; Nagy, T.; Reinhardt, C.; Knittel, V.; Bratschitsch, R.; Leitenstorfer, A.; Akemeier, D.; Hütten, A.; Kovacev, M.; Morgner, U. *Ann. Phys.* **2014**, *526* (3–4), 119–134.
- (45) Pfullmann, N.; Waltermann, C.; Noack, M.; Rausch, S.; Nagy, T.; Reinhardt, C.; Kovačev, M.; Knittel, V.; Bratschitsch, R.; Akemeier, D.; Hütten, A.; Leitenstorfer, A.; Morgner, U. *New J. Phys.* **2013**, *15* (9), 093027.
- (46) Berkovitch, N.; Ginzburg, P.; Orenstein, M. *J. Phys.: Condens. Matter* **2012**, *24* (7), 073202.
- (47) Awada, C.; Popescu, T.; Douillard, L.; Charra, F.; Perron, A.; Yockell-Lelièvre, H.; Baudrion, A.-L.; Adam, P.-M.; Bachetot, R. *J. Phys. Chem. C* **2012**, *116* (27), 14591–14598.
- (48) Palik, E. D. *Handbook of optical constants of solids*; Academic Press: Orlando, 1985.
- (49) Vasa, P.; Wang, W.; Pomraenke, R.; Lammers, M.; Maiuri, M.; Manzoni, C.; Cerullo, G.; Lienau, C. *Nat. Photon* **2013**, *7* (2), 128–132.